

Time-Resolved Particle Image Velocimetry within the Nozzle of a Drop-on-Demand Printhead

Jose Rafael Castrejón-Pita, Stephen Daniel Hoath[^], and Alfonso Arturo Castrejón-Pita
Inkjet Research Centre, University of Cambridge, 17 Charles Babbage Road, Cambridge, CB3 0FS, UK
E-mail: jrc64@cam.ac.uk

Neil Forbes Morrison
Department of Applied Mathematics, University of Leeds, Leeds, LS2 9JT, UK

Wen-Kai Hsiao[^] and Ian Michael Hutchings
Inkjet Research Centre, University of Cambridge, 17 Charles Babbage Road, Cambridge, CB3 0FS, UK

Abstract. Time-resolved particle image velocimetry (PIV) has been performed inside the nozzle of a commercially available inkjet printhead to obtain the time-dependent velocity waveform. A printhead with a single transparent nozzle 80 μm in orifice diameter was used to eject single droplets at a speed of 5 m/s. An optical microscope was used with an ultra-high-speed camera to capture the motion of particles suspended in a transparent liquid at the center of the nozzle and above the fluid meniscus at a rate of half a million frames per second. Time-resolved velocity fields were obtained from a fluid layer approximately 200 μm thick within the nozzle for a complete jetting cycle. A Lagrangian finite-element numerical model with experimental measurements as inputs was used to predict the meniscus movement. The model predictions showed good agreement with the experimental results. This work provides the first experimental verification of physical models and numerical simulations of flows within a drop-on-demand nozzle. © 2012 Society for Imaging Science and Technology.

[DOI: 10.2352/J.ImagingSci.Technol.12.56.5.050401]

INTRODUCTION

The study of droplet generation has recently attracted additional interest from researchers, motivated by its application in inkjet printing. Current drop-on-demand systems, in both commercially available and laboratory setups, allow the controlled generation of ink droplets, typically several picoliters in size, at kHz frequencies for graphical applications. For use in other markets, faster, more precise and more reliable systems are needed that can also deposit a wide range of liquids. Applications of inkjet technology may also be extended to markets dominated by other methods of liquid delivery, such as the printing of electronics, organic and biological materials, the dosing of drugs for pharmaceutical applications and the printing of high-viscosity liquids or molten metals for rapid prototyping. Good understanding of the process of jet and drop formation is fundamental to improving the quality and printing speed of drop-on-

demand systems. The physical properties of the working fluid (e.g., surface tension, viscosity, density, particulate content, viscoelasticity) together with the design of the printhead and the characteristics of the driving stimulus determine the behavior of the flow inside, and then outside, the nozzle. The mechanisms controlling jetting are varied, and range from acoustical effects to pure mechanical forces, as recently reviewed by Wijsoff.¹ In general, these effects can usually be controlled by the properties of the signal driving the printhead actuator (usually called the waveform).² In most commercial printheads the waveform is applied as an electrical voltage signal. Although several previous studies have analyzed the effect of waveform characteristics on drop formation, knowledge of the conversion of the driving signal to a pressure or velocity variation has remained elusive. This is mostly due to the experimental and technological challenges in measuring the actual pressure (or velocity) produced by the mechanical actuator when it is driven by a known electrical signal. Moreover, the response is expected to depend strongly on the design of the printhead and on the properties of the liquid. In addition to these complications, the size scale, nozzle geometry and operating speed of commercial printheads make measurements of pressures and/or liquid velocity difficult or even impossible.^{3,4} Although pressures and speeds have been measured in large-scale model systems by using highly sensitive pressure transducers and fluid anemometry techniques (January and March 2011 respectively), this and other laser-based approaches are not applicable to real printheads with multiple nozzles, as they would require optical access to the liquid inside the nozzle.^{3,4}

The objective of this work was to characterize the liquid movement inside a transparent printhead nozzle during jetting, by time-resolved velocimetry. The results of these measurements are then implemented as inputs in a Lagrangian numerical model, for comparison and validation.

[^] IS&T Members.

Received Dec. 20, 2011; accepted for publication Sep. 18, 2012; published online Jan. 21, 2013.

1062-3701/12/56(5)/050401/06/\$20.00

EXPERIMENTAL SETUP

The imaging setup, as shown in Figure 1, employed a Shimadzu HPV-1 ultra-high-speed camera which is ca-

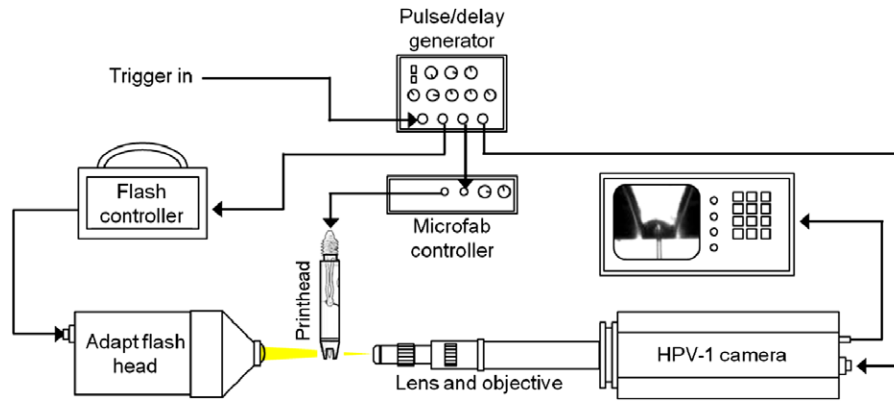
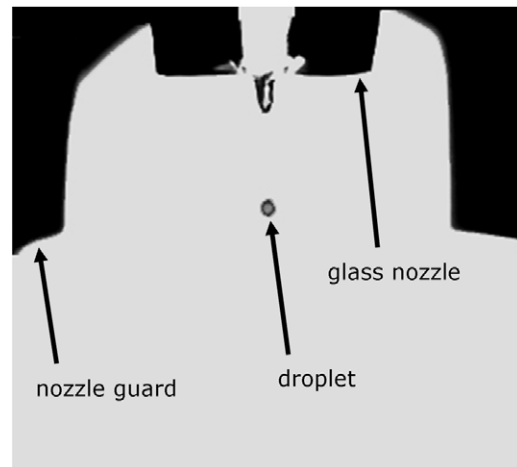


Figure 1. Experimental arrangement used in this work.

pable of capturing 102 full-resolution gray-scale images (310×260 pixels) at up to 10^6 frames per second with exposure times down to $0.25 \mu\text{s}$. The illumination was provided by an Adapt Electronics Photoflash head which produces 500 J flashes of 2 ms duration. Illumination with the flash system is possible given the short total duration of the recording process ($100 \mu\text{s}$) and the relatively long duration of the flash pulse. To take account of the finite warm-up time of the light source and consequent strong variation in the illumination, triggering of the printhead and of the camera shutter were slightly delayed (by $\sim 100 \mu\text{s}$) relative to the trigger signal to the flash controller (CU-500) by using a delayed pulse generator (TTi TGP-110). This delay time ensured that images were recorded close to the time of peak illumination to achieve maximum contrast. In these experiments, images were recorded at 5×10^5 frames per second.

A single-nozzle drop-on-demand printhead with a piezoelectric ceramic actuator and a transparent glass nozzle with an exit diameter of $80 \mu\text{m}$ (MicroFab MJ-ABP-01-80-6MX) was mounted vertically on a motorized multi-axis positioning stage with its guarded nozzle directed downwards between the camera and the flash. The printhead was set to produce droplets at a speed of 5 m/s and a frequency of 7 kHz. The camera was fitted with a microscope lens (Navitar $12\times$ ultrazoom with Mitutoyo long working distance objective) to record shadowgraph images of the fluid. For better comparison with the numerical model, experiments were designed to study specific aspects of the liquid dynamics: the flow within the nozzle exit, the advancing meniscus and the formation of the jet and the upper part of the ligament and the subsequent recoil after ligament detachment. Figure 2 shows the region surrounding the nozzle outlet.

The liquid used in the present study was diethyl phthalate (DEP) with the following properties: density, $\rho = 1117 \text{ kg m}^{-3}$, viscosity, $\eta = 10 \text{ mPa s}$, and surface tension, $\sigma = 37.4 \text{ mN m}^{-1}$. DEP exhibits Newtonian (linear viscous) behavior. Jets were ejected from the printhead at a speed of $\sim 5 \text{ m s}^{-1}$ and at a repetition rate of 7 kHz. For particle image velocimetry (PIV), the fluid was seeded with TiO_2 particles with an average normal size of


 Figure 2. The tip of the printhead at low magnification. The nozzle guard is part of the printhead assembly; the nozzle diameter is $80 \mu\text{m}$.

$a = 2 \mu\text{m}$ and particle density $\rho_p = 800 \text{ kg m}^{-3}$, which were chosen for compatibility with the flow conditions as they must be able to follow the flow accurately and possess good reflective properties. The particle suspension was prepared as follows: TiO_2 particles were dispersed into 10 mL of warmed DEP, using a magnetic stirrer, and then the suspension was degassed in an ultrasonic bath for 15 min before loading into the printhead. Ideally, the concentration of particles should be high enough to guarantee that all the images contain enough particles to resolve the speed, but not so high that the images of the particles overlap in the image field.⁵ In these experiments, different particle concentrations ranging from 0.1 wt% to 0.3 wt% were tested. The 0.3 wt% concentration was used in the experiments presented here as it had a signal to noise correlation peak above 2:1. By applying Stokes' law⁴ to estimate the response time t_{response} from

$$t_{\text{response}} = 10\rho_p a^2 / 4\eta,$$

where ρ_p is the density of the particles, we estimated that these particles are able to follow changes in the flow with deviations of less than 1% for flows with timescales as short as $1 \mu\text{s}$, well above the expected frequencies encountered by the particles inside the nozzle ($\sim 2 \times 10^4 \text{ Hz}$).

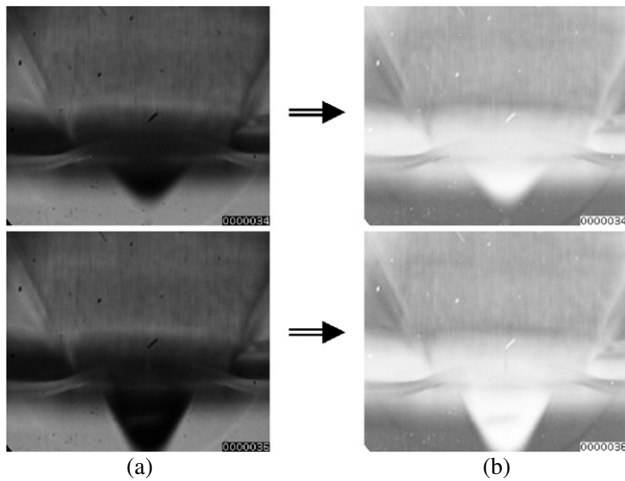


Figure 3. Gray-scale raw (a) and inverted (b) images acquired with the imaging system at full magnification. The nozzle exit is $80\ \mu\text{m}$ wide. As described in the text, for algorithm optimization all images were inverted before PIV analysis.

PARTICLE IMAGE VELOCIMETRY

Time-resolved digital particle image velocimetry (PIV) was used to extract quantitative velocity information about the flow inside the nozzle. Up to 102 consecutive images covering a complete jetting cycle were acquired with the high-speed camera. The PIV technique works by cross-correlating the intensity distributions of small subareas (called interrogation areas or boxes) of the flow in a pair of images with a certain time separation. By estimating the displacement vector for each interrogation area, in the known time interval, a velocity vector can be assigned for each of these interrogation windows. Unlike other particle tracking approaches, in PIV it is not necessary to resolve the motion of individual tracer particles, and hence the method is well suited to the analysis of flows with a large degree of spatial scale variation. In the current experiments the interrogation areas measured 32×32 pixels, and were analyzed by applying an interrogation-box overlap of 50% (typical in this kind of analysis⁵), giving an approximate box size in real space of about $13\ \mu\text{m} \times 13\ \mu\text{m}$, or a final spatial resolution of roughly $6.5\ \mu\text{m}$ (neglecting optical aberration caused by the nozzle geometry and refractive indices).

In conventional PIV systems, the flow under study is usually illuminated by high-intensity laser pulses of short duration. Each of these pulses illuminates the interrogation plane at different times and produces the illumination necessary to capture the averaged position of the seeded particles in the flow. A light sheet is usually produced by cylindrical lenses or more complex optical arrangements in such a way that only a thin layer of the fluid flow, and not the whole volume, is illuminated. For an axisymmetric flow field, imaging the central plane of the flow would in principle directly provide the information needed for the present purposes. However, it would be very difficult to generate a continuous sheet of laser light with the extreme thinness needed here, combined with the high intensity of illumination needed by the ultra-high-speed camera. The

use of a high-power pulsed laser is also not an option since the high pulse frequency needed surpasses the operating frequencies of available systems. Focusing high-intensity light into such a small volume could also have a number of undesirable consequences (e.g., high-temperature plasmas, thermal cracking of the glass, physical changes in the liquid, temperature increase, etc.). For these reasons, the fluid motion within the nozzle was captured by a shadowgraph imaging method. As a result, the measurements obtained by the PIV algorithms correspond to radially integrated velocities. The flow was back-illuminated with a long-duration flash and visualized by a microscope lens for which the depth of field ($\sim 200\ \mu\text{m}$) was comparable to the internal diameter of the nozzle. Therefore, in the recorded images, all the particles suspended within the nozzle are approximately in focus. Since the images were obtained by a shadowgraph technique the gray-scale images had to be inverted prior to application of the PIV analysis, since the software packages used are optimized for analyzing images that consist of white seeding particles in a black background. Two open-source PIV codes were used to analyze the images captured during the experiments, MatPIV 1.6.1 and URAPIV, with consistent results. Two raw images together with the inverted versions are shown in Figure 3. Figure 4 shows examples of PIV results superimposed as velocity vectors on images of the nozzle at various points in the jetting cycle. Regions of the image that were acquired by the camera but not of interest for velocity measurement were masked out and therefore excluded from the cross-correlation analysis performed by the PIV algorithms; the dotted line on the top-left image in Fig. 4 shows the mask layout.

By assuming a power-law radial velocity profile, it was possible to estimate the maximum velocity on the nozzle axis at the core of the flow. Eqs. (1) and (2) show respectively the general form of the n -power-law velocity profile $u(r)$ and the m -power particle density distribution $d(r)$ at radius r within a cylindrical tube of local radius R :

$$u(r) = \frac{n+2}{n} \left(1 - \left(\frac{r}{R}\right)^n\right) \quad (1)$$

$$d(r) = \frac{m+2}{m} \left(1 - \left(\frac{r}{R}\right)^m\right). \quad (2)$$

It can be easily shown that, for a central slice through a uniform density distribution of particles sampled across the nozzle profile (which corresponds to very large m), the averaged velocity is a fraction $n/(n+2)$ of the axial velocity. For Poiseuille flow, $n=2$, and the observed radially averaged value is one half of the axial speed. For higher values of n , or with a m -power-law particle density distribution, the radially averaged speed observed lies closer to the n -power-law axial speed by an extra factor of $(m+n+4)/(m+n+2)$. Thus the greatest difference between the radially averaged velocity and the value on the axis would be a factor of 2. From the whole velocity field, the average velocity at approximately $80\ \mu\text{m}$ above the nozzle outlet (from an area covering four velocity vectors) was extracted from 100 consecutive velocity maps

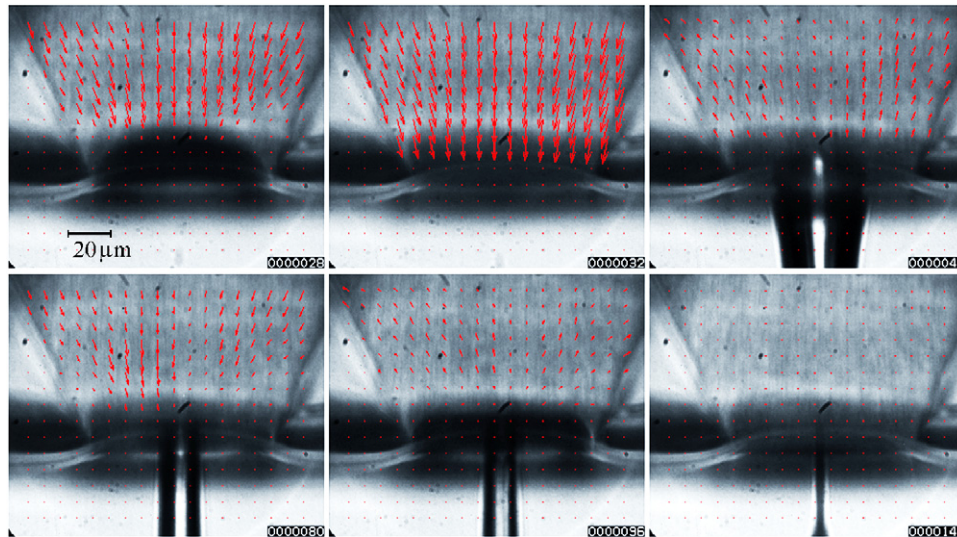


Figure 4. Images showing the velocity field inside the glass nozzle at various points during the jetting cycle. The dotted line in the first image shows the mask used for the PIV analysis. The fluid, DEP, contains $2\ \mu\text{m}$ TiO_2 particles. The image recording time shown in μs (microseconds) at the bottom right corner of each frame is offset by $140\ \mu\text{s}$ from the triggering of the first drop. The scale bar shown outside the glass is $40\ \mu\text{m}$. The top right-hand picture shows the effects of radial magnification caused by the refractive index of the glass: the jet emerging into the air is then close to its maximum width which is the same as the nozzle diameter ($80\ \mu\text{m}$), but the nozzle appears to be $\sim 50\%$ wider when viewed through the glass. The axial magnification effects are small because the external taper of the nozzle (well outside the field of view) is small and the refractive indices of the liquid and glass almost match.

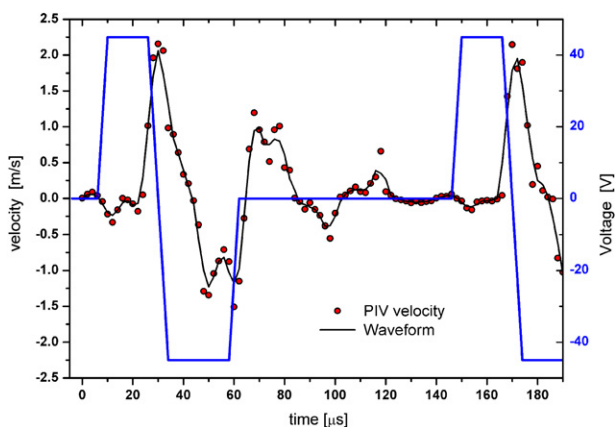


Figure 5. Time variation of the liquid velocity as measured by PIV within the nozzle on its axis (see text).

which covered one complete cycle of the jetting process. For this axial velocity essentially no radial correction was needed for distortion of the image, due to refraction at the air–glass and the glass–fluid interfaces. Axial correction due to the tapering nozzle profile is finite but effectively negligible on the micrometer scale, as shown for tapered cylindrical jets in a study of continuous fluid jets issuing from a nozzle.⁶ The axial velocity analysis can therefore be applied directly to image pixel data, on a linear scale determined by the actual nozzle exit diameter and by the pixel width of the exit as viewed in air (because the width viewed through the glass is magnified by refraction, as is clearly shown in the images in Fig. 3). The variation of axial velocity with time measured in this way is shown in Figure 5.

NUMERICAL SIMULATIONS

Simulations were performed by using computational numerical methods similar to those reported in Refs. 3 and 4. In brief, the numerical simulations used a Lagrangian finite-element method first developed for the study of creeping flow of dilute polymer solutions.⁷ The model assumes an axisymmetric flow, i.e., only the center plane of the jet is modeled. The method has since been extended to deal with inertial flows and used to model drop-on-demand printing of Newtonian and viscoelastic inks.⁶

The velocity and pressure fields were discretized over an irregular triangular mesh. An artificial stabilization was employed in order to prevent spurious numerical pressure oscillations.⁸ A theta scheme was used for the discrete time stepping, and the discrete governing equations were linearized via Picard iteration. Within each iteration, the linear system was solved numerically using the Minimal Residual Method (MINRES).⁹ Adaptive time stepping was controlled by a CFL (Courant–Friedrichs–Lewy) condition. The position of each mesh node (except those on the printhead inlet boundary) was updated after each time step using the converged velocity solution. To maintain element shape quality throughout the simulations, local mesh reconnections were made between time steps in regions where significant element distortion had occurred. The criteria for reconnection were based on the geometric optimality of the Delaunay triangulation.¹⁰ The local mesh resolution was also maintained by the addition of new nodes in depleted regions, and the removal of nodes in congested regions. In order to represent the capillary breakup of thin fluid threads, the fluid domain was subdivided artificially when the thread radius fell below a certain threshold (here

taken as $<1\%$ of the nozzle outlet radius). A more detailed discussion of the capability of the simulations to capture pinch-off dynamics on a finer scale is given in Ref. 3. No method of coalescence was implemented in the simulations.

A cylindrical coordinate system $\{r, \theta, z\}$ was used to describe the jet, with the origin taken as the center of the nozzle outlet. The governing equations are the Navier–Stokes equations, which we present below in their dimensionless form (taking the characteristic length scale to be the nozzle outlet radius $d/2$ and the velocity scale to be the target droplet speed v):

$$\partial u/\partial t + (u \cdot \nabla)u = -\nabla p + \nabla^2 u/\text{Re}, \quad \nabla \cdot u = 0,$$

where t , u , and p are the dimensionless time, fluid velocity, and pressure, respectively, and Re is the Reynolds number:

$$\text{Re} = \rho v d / 2\eta,$$

where ρ is the density and η the viscosity of the fluid, v the speed of jetting and d the nozzle diameter. Gravitational effects are negligible on the length scales considered in this study. The magnitude of gravity effects is estimated by the dimensionless Bond number, defined as

$$\text{Bo} = \rho g d^2 / 4\sigma,$$

where g is the acceleration of gravity and σ is the surface tension of the fluid. For the present experimental parameters Bo is less than 1.6×10^{-5} and so gravity effects may be neglected. Drag due to air resistance was also neglected in the simulations.

The shape of the printhead used in the simulations was chosen to replicate that of the MicroFab nozzle used in the experiments, while simplifying the interior of the printhead behind the nozzle. The initial finite-element grid is shown (horizontally) in Figure 6. The left boundary of the grid is the printhead inlet, at which a time-dependent plug flow velocity pulse $V(t)$ was imposed in the axial direction to represent the ink ejection mechanism in the experiments. The opposite boundary of the grid is the nozzle outlet. The initial shape of the fluid meniscus was flat, as in the experiments. The remaining curved boundaries of the grid are the rigid interior walls of the nozzle, at which no-slip boundary conditions were imposed. Axisymmetry about the z -axis (the jet axis) was assumed throughout. The boundary conditions at the free surface are those of zero shear stress and the interfacial pressure discontinuity due to the surface curvature

$$\hat{i} \cdot \tau \cdot \hat{j} = 0, \quad \text{and} \quad [\tau \cdot \hat{i}]_{\text{air}}^{\text{jet}} = -1/\text{We}(1/R_1 + 1/R_2)\hat{i},$$

where τ is the stress tensor, \hat{i} and \hat{j} are the unit normal and tangent vectors, R_1 and R_2 are the principal radii of curvature of the free surface, and We is the Weber number, defined as

$$\text{We} = \rho v^2 d / 2\sigma.$$

It was assumed that the external air pressure was a negligible constant. The location of the free surface was updated

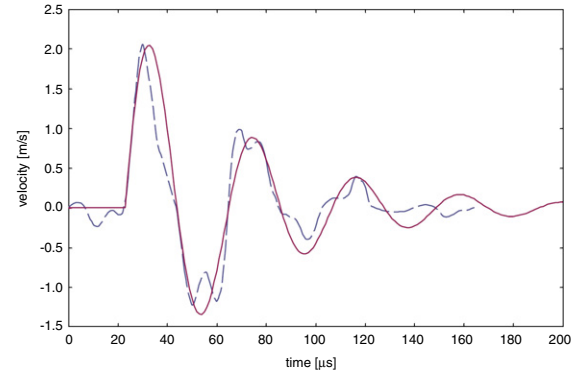


Figure 6. Comparison of a spline curve fitted to the measured PIV waveform with a damped sinusoidal curve, showing that the fluid motion in the nozzle after a drop is ejected primarily reflects viscous losses within the printhead. Simulations were performed with the spline curve fit as described in the text. The solid line corresponds to the model waveform input to the numerical code obtained from the experimentally obtained velocity waveform (dashed line).

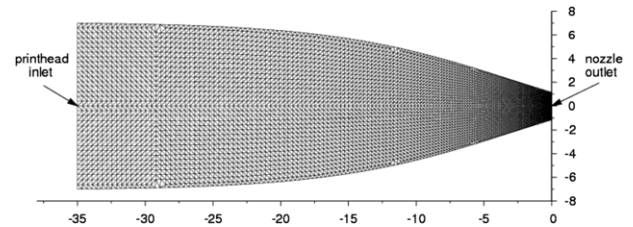


Figure 7. Initial grid used in simulations of a MicroFab MJ-ABP-01-80-6MX printhead. Axisymmetry is assumed. The unit of length is the nozzle radius $d/2 = 40 \mu\text{m}$.

automatically between time steps, since the finite-element mesh was Lagrangian and mesh nodes (including those on the interface) are advected with the local fluid velocity. The contact line between the interface and the interior walls of the nozzle was held pinned at the edge of the nozzle outlet. The fluid within the printhead was assumed to be initially at rest.

In order to generate droplets in the simulations, a time-dependent axial velocity pulse $V(t)$ was prescribed uniformly at the printhead inlet. While this was not expected to accurately model the experimental flow throughout the entire printhead, it was designed to produce sufficiently similar flow conditions in the vicinity of the nozzle cone to yield a reasonable correspondence between simulated and experimental drop shapes and speeds. The shape of the waveform pulse was represented by a spline curve fitted to the experimental velocity data obtained by PIV measurements as presented in Figure 7. Thus only the waveform of the PIV measurements was used directly as an input to the simulations. The calibration of the simulation drive velocity amplitude to the experimental conditions was done in terms of matching the initial jet tip speed that is measurable in the high-speed images. The amplitude of the waveform was then scaled appropriately to obtain the same drop speeds.

A selection of the results from the simulations using the experimentally extracted waveform pulse is presented in

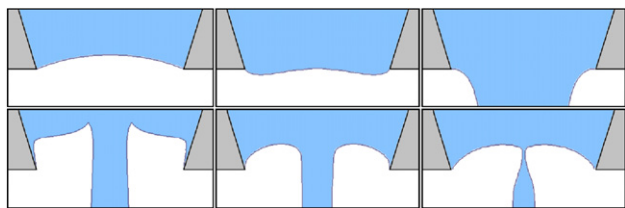


Figure 8. Fluid boundaries as calculated by Lagrangian simulations, at times consistent with those of the six images shown in Fig. 4. The unit of length is the nozzle radius $d/2 = 40 \mu\text{m}$.

Figure 8. These snapshots provide a direct comparison to the real meniscus positions shown in Fig. 4 as they represent the same relative times during the jetting cycle, and show good agreement.

DISCUSSION AND FINAL REMARKS

As observed in Figs. 4 and 8, good agreement between experiments and simulations was found. The meniscus shape and position and the necking behavior of the forming and collapsing filament agree well in both the experimentally obtained pictures and the numerically calculated figures. The code also correctly predicts the time to breakup ($\approx 142 \mu\text{s}$). This corroborates both the correctness of the numerical method (already proved in Ref. 4) and the successful extraction of the initial velocity and fluid boundary conditions needed to initialize the numerical Lagrangian code. In most other practical scenarios where commercial printhead systems are used, both the real velocity information and the initial conditions of the fluids (e.g., the position of the meniscus, or the precise nozzle geometry) are difficult or impossible to obtain, and therefore a similar approach cannot be performed. This is a major limitation of most industrial systems as any numerical method aiming to successfully predict the dynamics during drop ejection needs to be experimentally verified under ordinary conditions. Although the techniques discussed here require optical access to the flow inside the nozzle to obtain the dynamics of the flow during ejection, other methods such as vibrometry, ultrasonic velocimetry and X-ray particle image velocimetry may provide alternative routes to overcome these limitations. One of the major limitations of the experimental setup reported in this work is the use of a micrometer lens array with a depth of field similar to the external diameter of the printhead nozzle. Although conventional μ -PIV systems may produce depth of fields of the order of a few micrometers¹¹ (and therefore better spatial resolution), these systems usually operate at low frame rates ($\approx 2\text{k fpm}$) that would not resolve the dynamics of inkjet systems as they are restricted by the laser and/or the camera properties. Moreover, conventional μ -PIV systems could be more susceptible to optical distortions produced by refractive index differences between the outer medium, the nozzle and working fluid than the present method.

Particle image velocimetry has been applied to a similar system in the past,¹² but in that study flow repeatability was used to obtain the complete history of the jetting process. In this work, ultra-high-speed imaging has been used for the first time to overcome that limitation and time-resolved PIV measurements were made over the complete jetting cycle. Ultra-high-speed PIV has been successfully demonstrated for drop-on-demand jetting from tapered glass nozzles with an outlet diameter of $80 \mu\text{m}$, giving additional input for numerical simulations of inkjet printing performance. The accuracy of the present results is limited by the unknown radial distribution of the velocity and of the particles within the liquid, but can be shown to lie below the true axial velocity by a factor of <2 . The experimental measurements of velocity were used to provide initial conditions for Lagrangian simulations: these generated results for the meniscus shape and position which were in good agreement with experimental observations.

ACKNOWLEDGMENTS

This project was supported by the UK Engineering and Physical Sciences Research Council and industrial partners in the GlassJet and I4T projects (grant numbers EP/G029458/1 and EP/H018913/1). The Shimadzu HPV-1 camera and light sources were loaned from the EPSRC Instrument Loan Pool. Our thanks also go to Lisong Yang (Durham University, UK) for providing the TiO_2 particle materials.

REFERENCES

- H. Wijshoff, "The dynamics of the piezo inkjet print head operation," *Phys. Rep.* **491**, 77–177 (2010).
- A. U. Chen and O. A. Basaran, "A new method for significantly reducing drop radius without reducing nozzle radius in drop on demand drop production," *Phys. Fluids* **14**, L1 (2002).
- J. R. Castrejón-Pita, N. F. Morrison, O. G. Harlen, G. D. Martin, and I. M. Hutchings, "Experimental and Lagrangian simulations on the formation of droplets in drop-on-demand mode," *Phys. Rev. E* **83**, 036306 (2011).
- J. R. Castrejón-Pita, N. F. Morrison, O. G. Harlen, G. D. Martin, and I. M. Hutchings, "Experimental and Lagrangian simulations on the formation of droplets in continuous mode," *Phys. Rev. E* **83**, 016301 (2011).
- R. Adrian, "Particle imaging techniques for experimental fluid dynamics," *Ann. Rev. Fluid Mech.* **23**, 261 (1991).
- J. R. Castrejón-Pita, S. D. Hoath, and I. M. Hutchings, "Velocity profiles in a cylindrical liquid jet by reconstructed velocimetry," *ASME J. Fluids Engng.* **134**, 011201 (2012).
- O. G. Harlen, J. M. Rallison, and P. Szabo, "A split Lagrangian–Eulerian method for simulating transient viscoelastic flows," *J. Non-Newtonian Fluid Mech.* **60**, 81 (1995).
- N. F. Morrison and O. G. Harlen, "Viscoelasticity in inkjet printing," *Rheologica Acta* **49**, 619 (2009).
- C. Paige and M. Saunders, "Solutions of sparse indefinite systems of linear equations," *SIAM J. Numer. Anal.* **12**, 617 (1975).
- H. Edelsbrunner, "Triangulations and meshes in computational geometry," *Acta Numerica* **9**, 133 (2000).
- K. Shinohara, Y. Sugii, A. Aota, A. Hibara, M. Tokeshi, T. Kitamori, and K. Okamoto, "High-speed micro-PIV measurements of transient flow in microfluidic device," *Meas. Sci. Technol.* **15**, 1965 (2004).
- C. D. Meinhart and H. Zhang, "The flow structure inside a microfabricated inkjet printhead," *J. Microelectromech. Sys.* **9**, 67 (2000).